Composites: Part A 165 (2023) 107360

Contents lists available at ScienceDirect

Composites Part A

journal homepage: www.elsevier.com/locate/compositesa

Strain rate dependent compressive mechanical properties and dynamic failure of pre-strained epoxy syntactic foam

Longhui Zhang *, David Townsend

Department of Engineering Science, University of Oxford, Parks Road, Oxford OX1 3PJ, U.K

ARTICLE INFO

Keywords:
Syntactic Foam
Pre-strain
Collapsed Microballon
Dynamic failure

ABSTRACT

Syntactic foam is increasingly used in engineering applications. This paper studies the dynamic mechanical properties and failure of syntactic foam, with emphasis on the influence of pre-strain and the embedded collapsed microballons. The epoxy syntactic foam (ESF) with different levels of pre-strain is successfully produced using a confinement sleeve technique. The initial and pre-strained ESF are tested and compared from quasi-static to high strain rates about 1000 /s. The dynamic deformation processes of the initial and pre-strained ESF are monitored using high speed photograph techniques. The stress–strain relationships of the initial and pre-strained ESF show different strain rate dependence. The pre-strained ESF presents good deformability. The dynamic failure of the ESF results from shear strain localization, regardless of the pre-strain. The initial ESF shows macro elastic brittle behaviour, and the fracture surface consists of partially deformed and localized regions. The produced ESF with pre-strain, however, presents the collapsed microballons surrounded by the flow like behaviour of the severely deformed matrix, which would be associated with the thermomechanical coupling process. This study indicates the ESF with embedded collapsed microballons shows deformability and high energy absorption capacity.

1. Introduction

Syntactic foam, which consists of the microballons embedded in the polymeric matrix, is increasingly employed in automobile, marine and aerospace engineering applications [1–3]. With the interest in light weight components, the use of syntactic foam is an important design approach [4]. The syntactic foam can be a core material in the sandwich structures [5–8]. The increasing demand for light weight and protective composite structures under impact loading stimulates the study of dynamic behaviour of syntactic foam.

A number of available studies [9–11] focused on the mechanical properties of syntactic foam under quasi-static condition. The bulk mechanical responses were quantitatively described by Gupta et al. [12,13]. Kim et al. [14] produced the syntactic foams with various densities and reported different failure mechanisms of the syntactic foams under quasi-static compression. The influence of different factors, including the cell structure, the porosity on the bulk mechanical behaviour can be found in Refs. [15–17]. Doddaman et al. [18–20] pointed out the influence of surface treatment on quasi-static compression behaviour of syntactic foams. It's found that the syntactic foams reinforced with surface modified cenosphere presented superior properties and energy absorption. Recently, Carolan et al. [21] developed a novel numerical method to predict the fracture strength as a function of microballon volume fraction. It's shown that the variation in fracture strength is linked to the randomness of the underlying geometry. Although the quasi-static response of syntactic foam has been widely reported, studies on the mechanical response at high strain rates are required for the analysis of impact events [22–25]. Li et al. [26] reported the flow and failure of an epoxy syntactic foam (ESF) from quasi-static to high strain rates using the split Hopkinson pressure bar (SHPB) [27–30]. In addition to the uniaxial loading, the lateral confinement was found to influence the compressive response of ESF from quasi-static to high strain rates [31]. Gupta et al. [32] studied the dynamic behaviour of various syntactic foams under uniaxial compression using the SHPB technique. The dynamic compressive strengths were found to be significantly higher than the quasi-static strength. The Taylor rod impact test was conducted by Rittel [33] to investigate the adiabatic shear failure of syntactic foam at higher impact velocities. The forefront of ESF for functional and structural applications, and the compressive properties, fracture and impact toughness of ESF can be found in a recent review of Anirudh et al. [34].

An exceptional and novel method, developed by Gupta et al. [35], is

* Corresponding author.
E-mail addresses: lhzhang.mechanics@gmail.com, longhui.zhang@eng.ox.ac.uk (L. Zhang).

https://doi.org/10.1016/j.compositesa.2022.107360
Received 4 July 2022; Received in revised form 17 November 2022; Accepted 30 November 2022
Available online 6 December 2022

able to repeatedly load the material at a given strain rate until failure. The master stress–strain graph, which was measured from the stress–-strain relationship in each cycle, can be used to reveal the rate dependent failure mechanism, such as the matrix cracking and shattering along with plastic deformation of the matrix. Recently, Kim et al. [36] also highlighted that the pre-strain changed the deformation mechanism of the foam. Liu and Subhash [37] compared the polymeric foams subjected to monotonic loading and incremental loading under uniaxial strain condition [38]. The pre-strained foam was pushed out of the confinement sleeve for visual observation. However, the mechanical response and the microstructure of the pre-strained foam are yet to be studied. In the aerospace industry, the syntactic foam can be used as structural components in aircraft and space shuttle, see the works of Walker and Chocron [39,40] in SWRI on discovery of the Columbia space shuttle. The syntactic foam can become a layered material between the fan containment casing and the fan blade tip of jet engine. The syntactic foam can also be used as a core material in the sandwich structure of the fan containment casing [41–43]. The foam would deform during assembly processes [42,44], particularly after a certain period of service arising from the fan blade tip. Likewise, a syntactic foam component loaded by a projectile consists of the collapsed microballons. This deformed foam is different from the initial foam. However, specific studies on the flow and failure of the pre-strained syntactic foam, are still less reported, including their dependence on the strain rate. These are important to provide further insight into the energy absorption and the crushability map of the foam in the following impact events.

In this work, with the assistance of Digital Image Correlation (DIC) technique [8,45,46], the flow and failure of an ESF with and without pre-strain are compared at high strain rates of 1000 /s. Likewise, the corresponding constitutive responses from quasi-static to high strain rates are also characterized. The materials and the experimental protocols are introduced in Section 2. Section 3 shows the experimental results, followed by the discussion in Section 4 and the conclusion in Section 5.

2. Experimental protocol

2.1. Materials

The investigated ESF consists of a thermoset epoxy matrix and amorphous silicate-based glass microballons with an average wall thickness of 1.10 μm and an average diameter of about 42 μm. The ratio of the volume occupied by the microballons and the total bulk volume of the foam is approximately 0.5. The ESF has a density of 715 kg/m^3. The relevant material properties can be found inRef. [47]. The supplied ESF rod was machined to the cylindrical specimens (5 mm length and 5 mm diameter). The pre-strained ESF was produced under quasi-static uniaxial strain condition with the assistance of a rigid confinement tube [37]. This technique is adopted here with a very different purpose,that is, to produce the ESF with pre-strain. Fig. 1 schematically shows the loading process at different strain levels. An adapter is placed on the top to apply the compressive loading to the ESF. The surface treatment has been reported to influence the properties of syntactic foam [18–20]. In the current work, only the grease lubrication was used between the confinement tube and the ESF. No other surface preparations were carried out between the confinement tube and the ESF. The typical engineering stress–strain relationship during the pre-strain loading process is shown in Fig. 2. The three stages include linear elastic, plastic region and densification. The densification strain is determined by the strain corresponding to the maximum energy efficiency [48,49]. Three pre-strain levels are defined. They correspond to the pre-strain of 0.10, 0.29 and 0.48 respectively. These three strain levels are defined as pre-strain level 1, pre-strain level 2 and pre-strain level 3. The pre-strain levels are inspired by the issues related to densification [50]. The three pre-strain levels correspond to 24 %, 70 % and 117 % of the densification strain. With the initial foam (0 % of the densification strain), this work systematically reports the mechanical behaviour and energy absorption of ESF with different pre-strain levels.

Fig. 3 compares the microstructures of the initial ESF and the pre-strained ESF, using a Carl Zeiss Evo LS 15 VP-Scanning Electron Microscope (SEM). The microstructure of the initial ESF (Fig. 3a) shows the microballons distributed in the epoxy matrix. The bulk density of the ESF increases to about 745 kg/m^3, 1175 kg/m^3 and 1545 kg/m^3 after three levels of pre-strained deformation. This is similar to the increase of

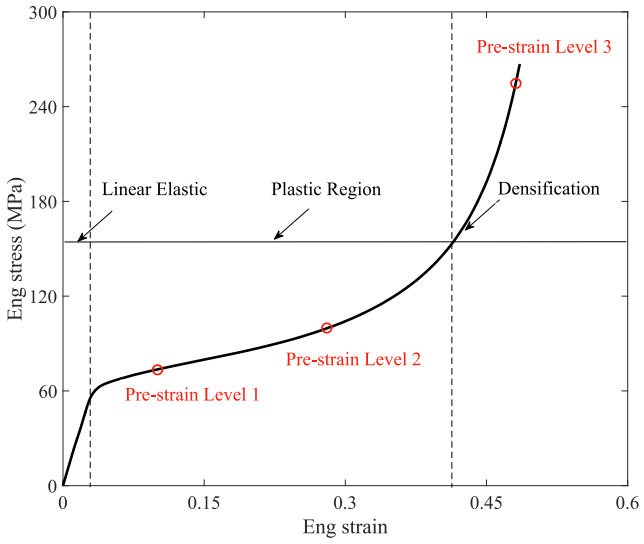

Fig. 2. Typical stress–strain relationship of the ESF under quasi-static uniaxial strain condition. Three pre-strain levels are marked.

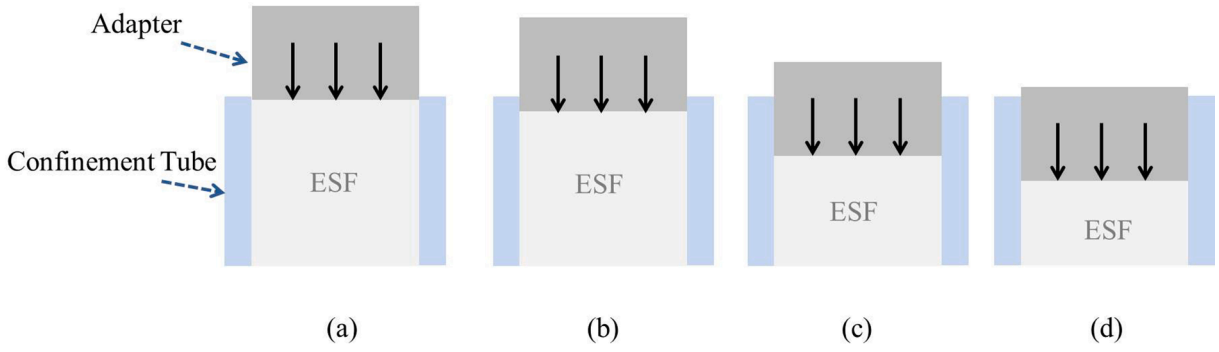

Fig. 1. Schematic of production process of the pre-strained foam (a) Initial ESF (b) ESF with pre-strain level 1 (c) the ESF with pre-strain level 2 (d) the ESF with pre-strain level 3.

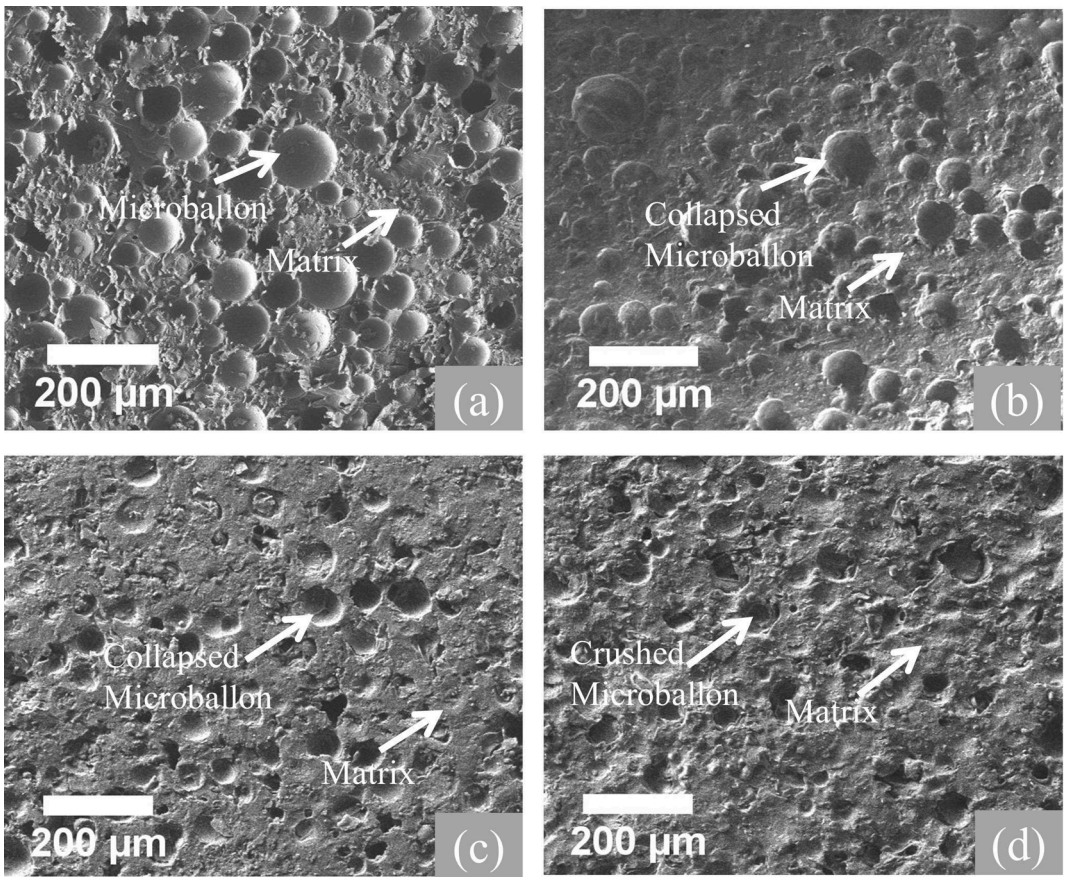

Fig. 3. SEM images of (a) ESF without pre-strain (b) ESF with pre-strain level 1 (c) the ESF with pre-strain level 2 (d) the ESF with pre-strain level 3.

density of the pre-strained foam [37]. As reported by Gupta et al. [51,52] and Irven et al. [53], the density significantly affects the mechanical behaviour of syntactic foam. Assuming that the reduced volume of the bulk foam is solely due to the failed microballons, the estimated volume fraction of the failed microballons decreases to 48 %, 18 % and about 0 % after three levels of pre-strained deformation.

Fig. 3(b-c) show the microstructures of the ESF with pre-strain level 1 and 2, which consists of the collapsed microballons. As can be seen in Fig. 3d, the further deformation at pre-strain level 3 results in a more significant compaction of the microballons. These are different from the microstructure of the initial ESF.

Computer aided tomography (micro CT-scan) is also a useful tool to reveal the internal microstructural change of the syntactic foam [32,54,55]. The X-ray microtomography of the ESF is characterized by North Star Imaging-X-ray System. Compared to the evenly distributed microballons in the initial ESF in Fig. 4a, the increase of pre-strain results in the collapse of the microballons [55], as can be seen from the gradual spase distribution of the microballons in Fig. 4(b-c). At the pre-strain level 3, a significantly reduced portion of the collapsed microballons is shown in Fig. 4d due to microballoon crushing. The SEM and micro CT-scan characterizations also show that, except for the collapsed and crushed microballons, no micro cracks are in the epoxy matrix in the pre-strained ESF. This is similar to the observations in the X-ray microtomography of the deformed ESF [55].

2.2. Mechanical testing apparatus

The compressive tests at quasi-static 0.01 /s and medium strain rate of 10–15 /s were performed using a screw driven Zwick 050 machine and a hydraulic Instron machine 8854. The macro engineering strain of the ESF specimen was measured from the relative motion of the load platens painted with speckle pattern. The images were recorded by using a phantom camera and subsequently analyzed by a commercial DIC software Lavision Davis. The high strain rate tests (about 1000 /s) were performed using a 16 mm diameter SHPB [56–59]. Fig. 5 schematically shows the SHPB setup. The incident bar and transmitted bar are made from Ti6Al4V alloy. Both bars are 2.7 m long. The length of the Ti6Al4V strike bar is 2.5 m. The dynamic deformation of the ESF was monitored by using a high speed Kirana camera at a frame rate of 200, 000 fps. The high speed images were processed by a Least-Squares Matching algorithm [60] in the DIC analysis. The matching was based on a 6th order spline sub-pixel image interpolation scheme and an affine shape function [61] available in Lavision Davis. The pulse shaper is made from a neoprene rubber sheet with thickness of 0.7 mm-1 mm. The pulse shaper helps to achieve the force equilibrium of the specimen and increase the rise time of the incident wave.

3. Experimental results

3.1. Experimental results at quasi-static and medium strain rate

After the pre-strained loading, the ESF was pushed out of the confinement tube and subsequently subjected to the compressive testing. Fig. 6 compares the stress–strain relationships of the initial and pre-strained ESF. The stress of the initial ESF decreases beyond the peak stress of 52 MPa. This is followed by strain softening, and densification at a strain of about 0.63. The ESF with pre-strain level 1 presents a reduced slope in the initial part of the stress–strain curve. After the peak stress of 49 MPa, the ESF with pre-strain level 1 shows strain hardening, with a slight drop of stress at a strain of about 0.40. The stress values of the ESF with pre-strain level 2 and pre-strain level 3 continue to increase, with a slight drop at a strain of 0.48–0.54. The stress increases

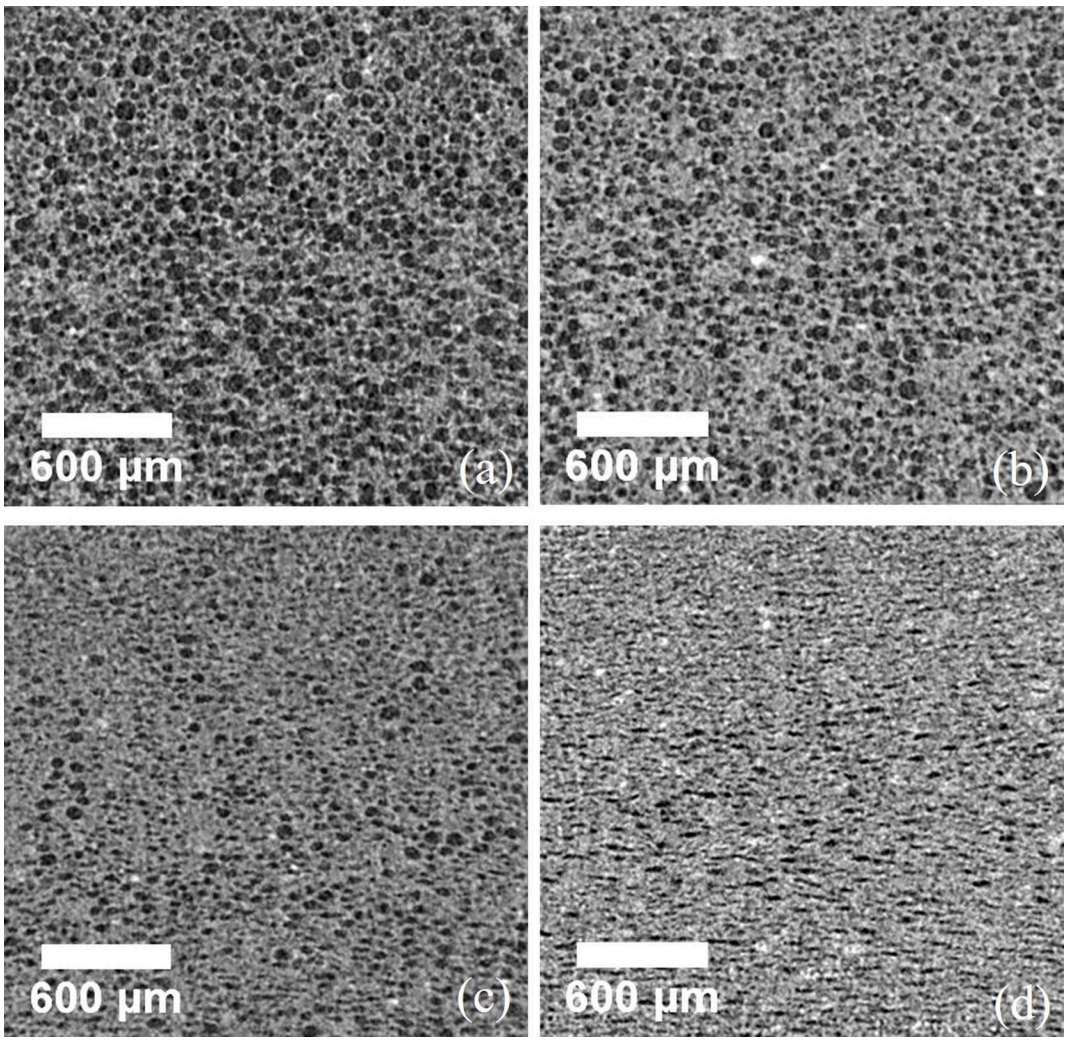

Fig. 4. Two dimensional slices from the X-ray CT three dimensional reconstruction of (a) ESF without pre-strain (b) ESF with pre-strain level 1 (c) the ESF with pre-strain level 2 (d) the ESF with pre-strain level 3.

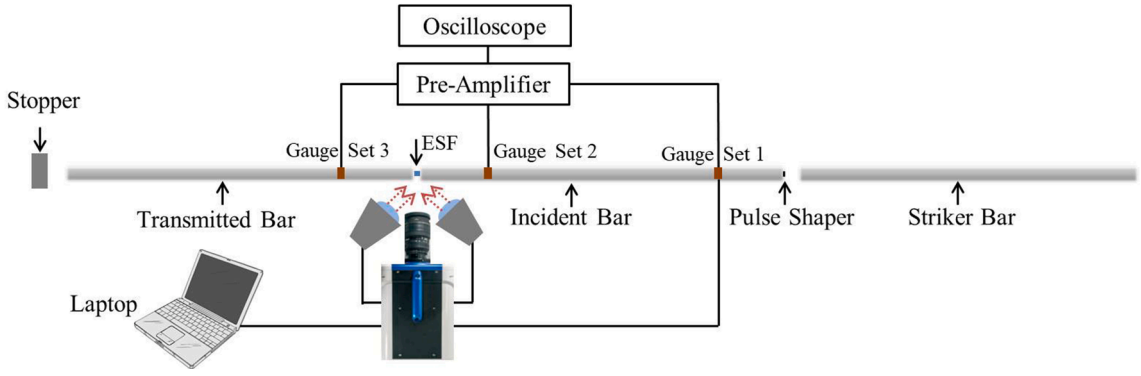

Fig. 5. SHPB setup for the compressive tests at high strain rates.

dramatically in the densification stage.

Fig. 7 presents the stress–strain relationships of the initial ESF and pre-strained ESF at medium strain rate of about 10–15 /s. To protect the load platens of the Instron machine, the applied displacement was carefully controlled. This corresponds to a maximum strain of 0.66–0.8. The initial ESF shows a peak stress of 57 MPa. Subsequently, the strain softening appears until a densification strain of 0.7. After the peak stress of 59 MPa, the ESF with pre-strain level 1 shows a decrease of stress. However, no strain softening can be seen in the stress–strain relationships of the ESF with pre-strain level 2 and pre-strain level 3, except for a slight drop of stress at a strain of about 0.45.

3.2. Experimental results at high strain rate

Fig. 8a presents the typical stress wave signals of a pre-strained ESF. Since the length of the Ti6Al4V strike bar (2.5 m) is comparable to that

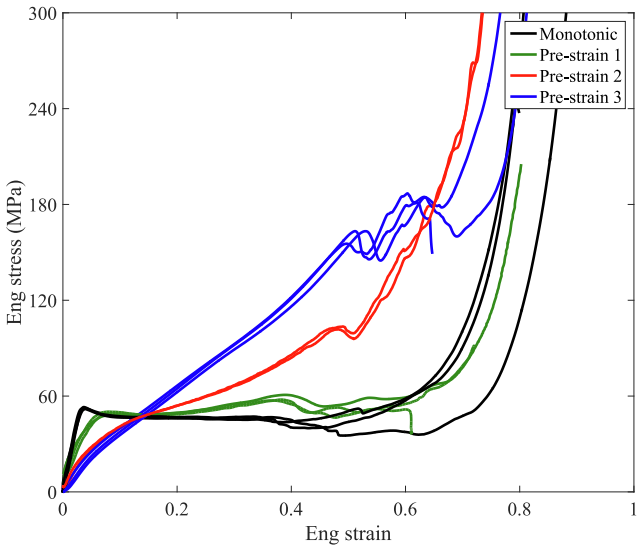

Fig. 6. Comparison of the constitutive relationships of the initial and pre-strained ESF at quasi-static loading.

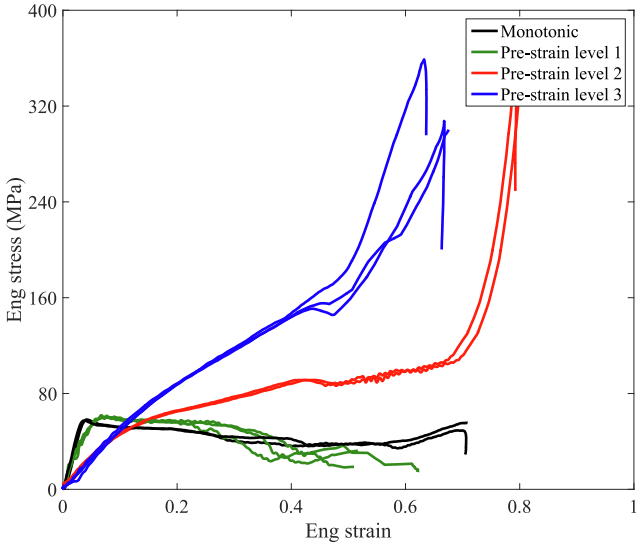

Fig. 7. Stress–strain relationships of the initial and pre-strained ESF at medium strain rate of 10–15 /s.

of the incident bar, two strain gauge sets (1 and 2) are attached to the incident bar to separate the superimposed waves. The strain gauge set 3 is on the transmitted bar. The stress wave analysis can be found in the work of Quino et al. [59] and not repeated here. The input and output forces are compared in Fig. 8b. The force equilibrium is achieved at a constant strain rate of approximately 1200 /s. The stress of the specimen is measured directly from the output force.

Fig. 9 presents the constitutive relationships of the initial and pre-strained ESF at high strain rates. After the initial part and the peak stress of 70 MPa, the stress of the initial ESF shows a rapid decrease. The ESF with pre-strain level 1 presents a decrease of stress after the peak stress of 66 MPa. However, the ESF with pre-strain level 2 shows more deformability with a nonlinear increase of stress up to a strain of 0.33. The corresponding peak stress of 90 MPa is higher than that of the ESF without pre-strain or pre-strain 1. The ESF with pre-strain level 3 also shows large deformation and a maximum stress of about 150 MPa. Beyond the maximum stress, the stress of pre-strained ESF decreases rapidly. Considering three pre-strained levels of 0.1, 0.29 and 0.48, the

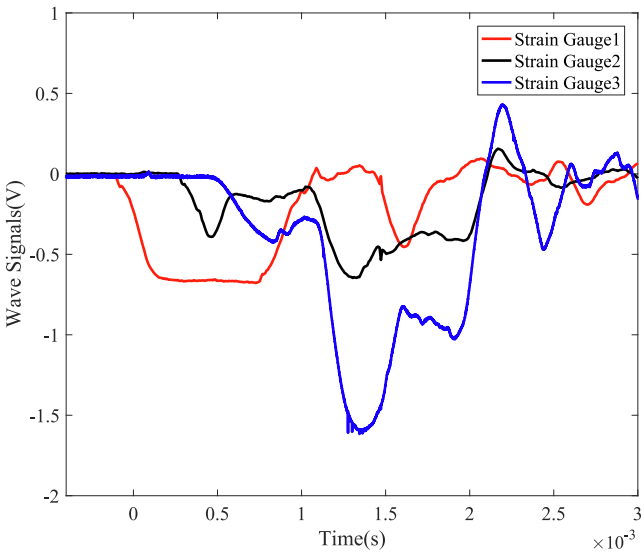

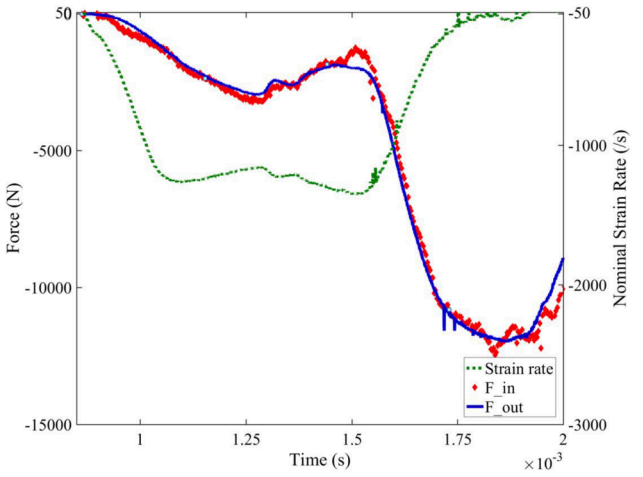

Fig. 8. Typical raw data from the SHPB setup (a) Stress wave signals (b) Force equilibrium and the corresponding strain rate history.

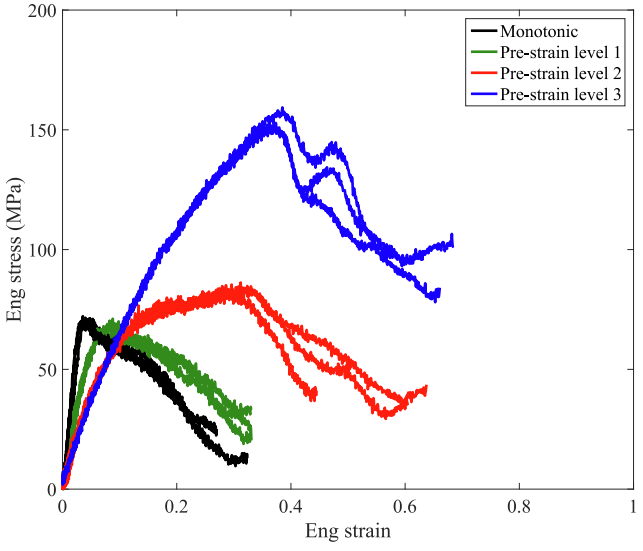

Fig. 9. Stress–strain relationships of initial and pre-strained ESF at high strain rate of 900–1200 /s.

final dynamic failure strain values of the pre-strained ESF are 0.19, 0.62 and 0.85. Such high failure strain values clearly indicate the improved deformation capacity of the pre-strained foam.

Fig. 10a and Fig. 10b show the stress–strain curves of the ESF without pre-strain and the ESF with pre-strain level 1 at different strain rates. A strain rate dependence can be seen from the amplification of peak stress. Beyond the peak stress, the stress at high strain rate drops rapidly at a strain of 0.05 for the initial ESF and at a strain of 0.09 for the ESF with pre-strain level 1.

Considering the ESF with pre-strain level 2, Fig. 10c compares the stress–strain curves from quasi-static to high strain rates. The pre-strain significantly improves the deformability of the ESF. With the increase of strain rate, the flow stress increases at corresponding strain values. The stress–strain curve at high strain rate shows a rapid drop at a strain of 0.33. This is different from those at quasi-static and medium strain rate. Fig. 10d shows the effect of strain rate on the constitutive response of the ESF with pre-strain level 3. Compared to the ESF with pre-strain level 2, the ESF with pre-strain level 3 shows higher flow stress. This indicates the pre-strain not only improves the deformability but also increases the flow stress. Different from the slight load drop at a strain of 0.46–0.49 at quasi-static and medium strain rate, the stress–strain curve at high strain rate shows a rapid load drop beyond a strain of 0.37.

Fig. 11a and Fig. 11b show the typical stress histories of the ESF without pre-strain and with pre-strain level 1 at high strain rate of 1000 /s. Fig. 12a and Fig. 12b reveal the deformation process recorded by the high-speed camera. After the homogeneous deformation at stage 2, the strain localization (white arrow) starts at stage 3. The intensive strain localization and the decreasing stress can be seen at stage 4 in the initial ESF. As the deformation continues, the cracks propagate at stage 5. Except for the initial homogeneous deformation, the ESF without pre-strain shows brittle behaviour due to the early strain localization. For the ESF with pre-strain level 1, the failure originates from the bottom of the specimen at stage 3. This is accompanied by the strain (stress) concentration at two specimen ends at stage 4 and the crack propagation at stage 5.

Fig. 11c shows the stress as a function of time for the ESF with pre-strain level 2. The corresponding high speed images are shown in Fig. 12c. The initial part of the stress history changes beyond the stress of 75 MPa. The uniform deformation can be seen at stage 2. A slight strain localization (marked by a white arrow) appears close to the right end of the specimen at stage 3. The further compression results in the strain localization at stage 4. The crack follows this strain localization path at stage 5, resulting in the fracture of the specimen.

Fig. 11d shows the stress history of the ESF with pre-strain level 3 at high strain rate of 1200 /s. The deformation process analyzed by the DIC is given in Fig. 12d. The flow stress increases to the peak stress at stage 3. Before the peak stress, a uniform deformation can be observed at stage 2. A strain (stress) concentration exists at the end of the specimen. However, the failure initiates from the centre of the slightly barreled specimen at stage 3. This is also followed by the strain localization at stage 4 and the crack propagation at stage 5.

The initial ESF presents elastic-brittle behaviour at higher strain rates. Fig. 13a shows the strain rate effect on the consistent initial peak stress of the ESF without pre-strain and pre-strain level 1. For the ductile ESF with pre-strain level 2 and pre-strain 3, the flow stress at a given strain of 0.2 as a function of strain rate is plotted in Fig. 13b. The influence of strain rate on the flow stress is described by a power law model:

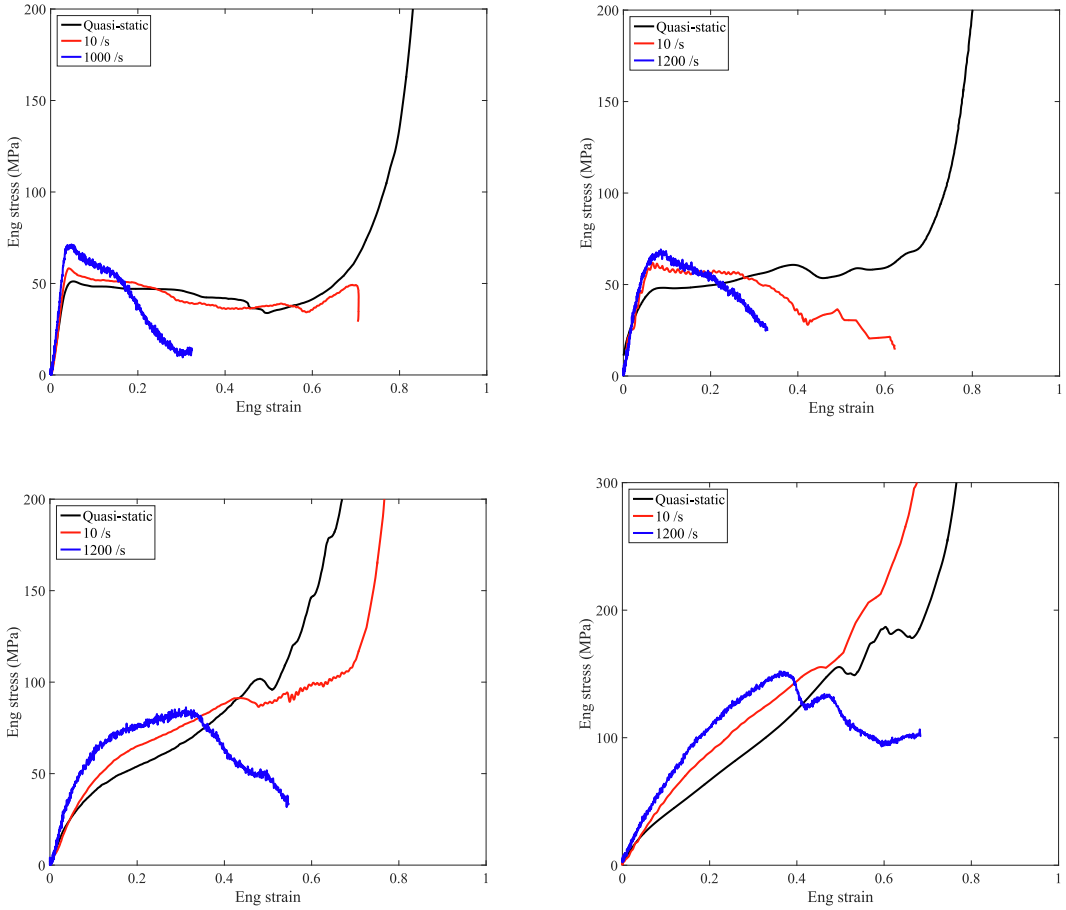

Fig. 10. Stress–strain curves of (a) the initial ESF, (b) the ESF with pre-strain level 1, (c) the ESF with pre-strain level 2 and (d) the ESF with pre-strain level 3 from quasi-static to high strain rates.

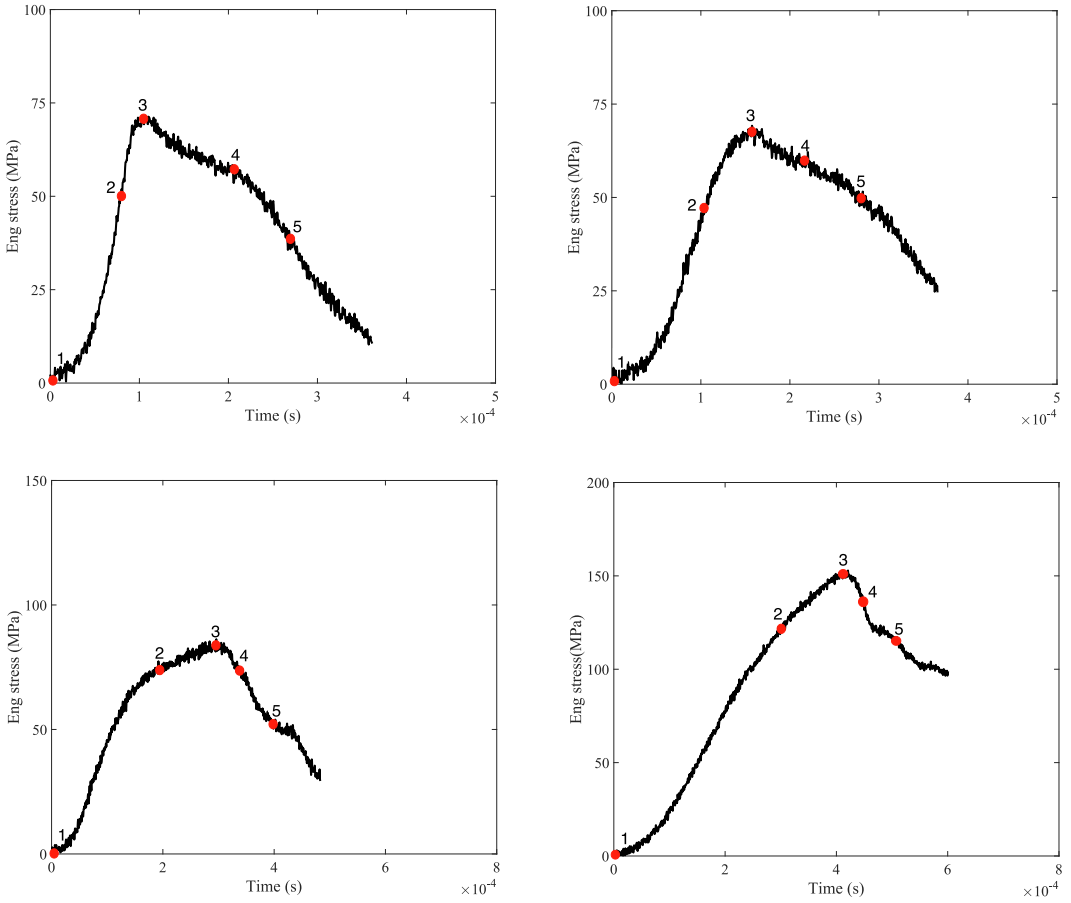

Fig. 11. Stress history of the ESF (a) without pre-strain, (b) with pre-strain level 1, (c) pre-strain level 2 (d) and pre-strain level 3.

$$\sigma = \sigma_{ref}\left(\frac{\dot{\varepsilon}}{\dot{\varepsilon}_{ref}}\right)^{c} \tag{1}$$

Here,σ_{ref} is the reference flow stress, $\dot{\varepsilon}_{ref}$ is equal to 0.01 /s which is the reference strain rate, the parameter C reveals the strain rate dependence. Fig. 13 shows the comparison of the experimental data and the model description. The parameter C is between 0.026 and 0.03 for the initial ESF, the ESF with pre-strain level 1 and 2. The parameter C increases to 0.0399 for the ESF with pre-strain level 3. The ESF with large pre-strain seems to show more significant strain rate sensitivity.

The energy absorption under impact is of considerable interest to engineers. Fig. 14 shows the energy density of the initial ESF and the pre-strained ESF at different strain rates. The energy density is calculated by the area under the stress–strain curve up to the densification ($W = \int \sigma d\varepsilon$). In general, the energy density of the pre-strained ESF is higher than that of the initial ESF, regardless of the strain rate. This indicates the energy absorption of the ESF is improved by the pre-strain. The energy density of the initial ESF and the ESF with pre-strain level 1 decreases from quasi-static to high strain rates. The energy density values of the ESF with pre-strain level 2 and level 3 are comparable at quasi-static and high strain rates, except for a moderate variation at medium strain rate. The comparison of energy absorption illustrates the brittleness of the ESF is gradually suppressed with the pre-strain.

The density is an important parameter to describe the mechanical behaviour of syntactic foam, as can be seen in the studies of Gupta et al. [51,52] and Irven et al. [53]. Here, the specific energy absorption $\frac{\int \sigma d\varepsilon}{\rho}$, which is the strain energy density ($\int \sigma d\varepsilon$) divided by the foam density ρ, is compared in Fig. 15 to illustrate energy-mass issue of the ESF at different strain rates. The specific energy absorption is comparable for the ESF with a similar density of 715–745 kg/m^3. A different trend at high strain rates can be observed in the ESF with higher densities. For instance, the specific energy absorption is about 20 kJ/kg for the initial foam and the ESF with a similar density of 715–745 kg/m^3. However, the specific energy absorption increases to 28 kJ/kg in the ESF with a higher density of 1175 kg/m^3, and increases to 45 kJ/kg in the ESF with a highest density of 1545 kg/m^3. Consequently, the specific energy absorption also shows that the deformation capacity of the pre-strained ESF is gradually improved, particularly under impact loading condition.

3.3. Microstructural characterization

The fracture morphology of dynamically failed ESF specimens was characterized. The fracture surface of the initial ESF consists of the partially deformed region and the localized region (white arrow in Fig. 16a) with collapsed microballos. This corresponds to the strain localization induced brittle failure of the initial ESF. For the pre-strained ESF, the fracture surfaces in Fig. 16(b-d) are characterized by evenly distributed fractured microballons with debris [12,62,63].

Fig. 17 presents the magnified fracture surfaces of the dynamically failed ESF shown in Fig. 16. Specifically, the initial ESF shows the fractured microballons and the almost intact microballons (white arrow in Fig. 17a) embedded in the matrix (dashed arrow in Fig. 17a). For the pre-strained ESF, the microballons are not clearly visible. The fracture surface of the ESF with pre-strain level 2 shows a microballon covered by the debris [63], as shown in Fig. 17b. The fracture surface of the ESF with pre-strain level 3 consists of partially fractured microballons surrounded by the matrix with debris (Fig. 17c). A closer view of the dashed rectangle area in Fig. 17c is provided in Fig. 17d. The matrix (white color filled arrow) shows the flow like characteristics.

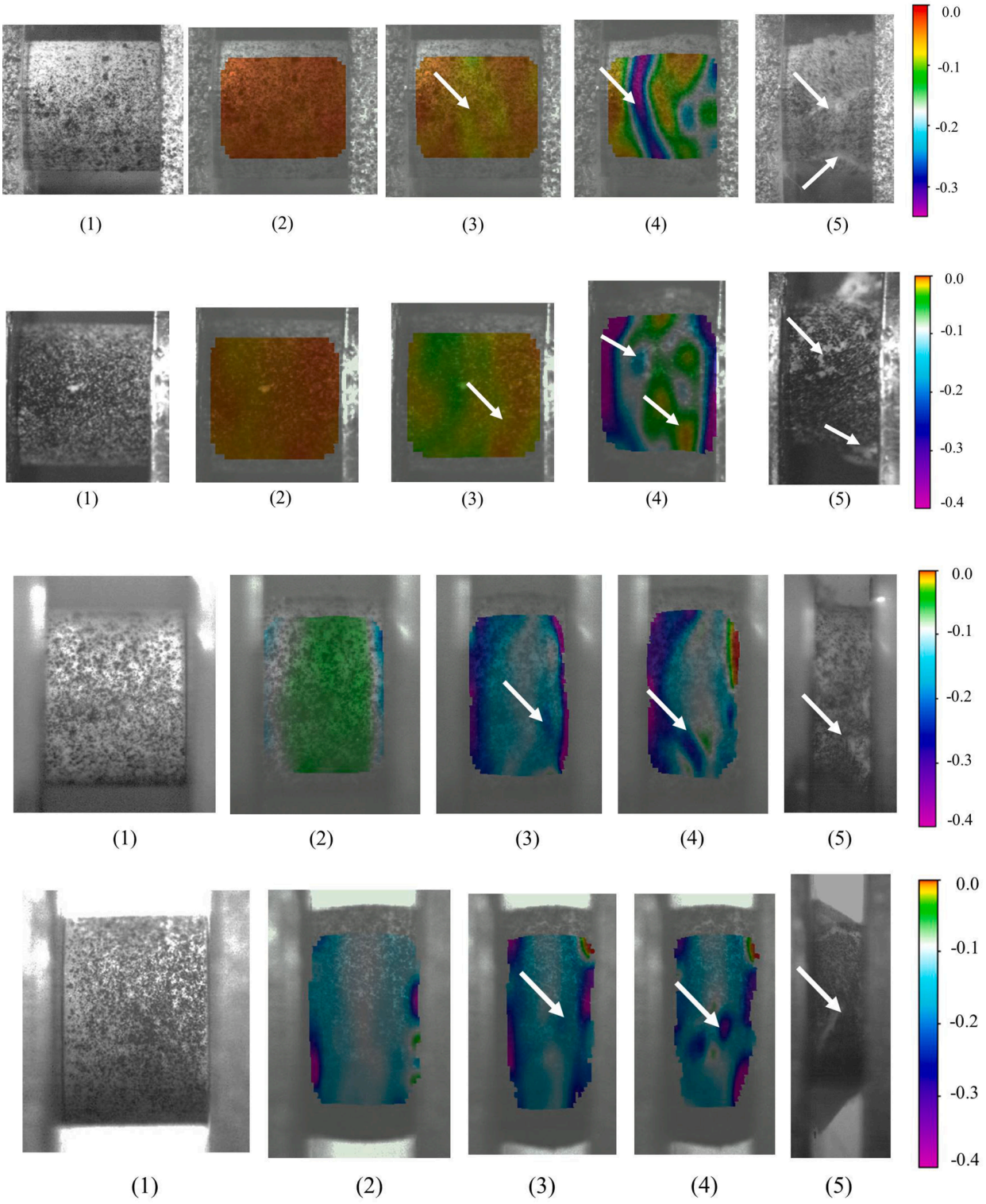

Fig. 12. High speed deformation process (axial engineering strain contour from DIC analysis is given) of the ESF (a) without pre-strain, (b) with pre-strain level 1, (c) pre-strain level 2 (d) and pre-strain level 3. Note that a slight barreling occurs during the dynamic deformation for the ESF (b) with pre-strain level 1, (c) pre-strain level 2 (d) and pre-strain level 3.

4. Discussion

With the increasing interest in the light weight and impact resistant aircraft structural components, the use of polymeric syntactic foam is an important design strategy. The syntactic foam used as structural components would be subjected to deformation in service, for instance, loaded by a projectile. However, the information on the microstructure and the mechanical behavior of the pre-strained syntactic foam, are rarely reported in the literature, except for the recent studies of Kim et al. [36] and Sanborn et al. [64]. These are important to understand the final crushability of the foam in the following impact events. This paper investigates the dynamic flow and failure of ESF with three levels

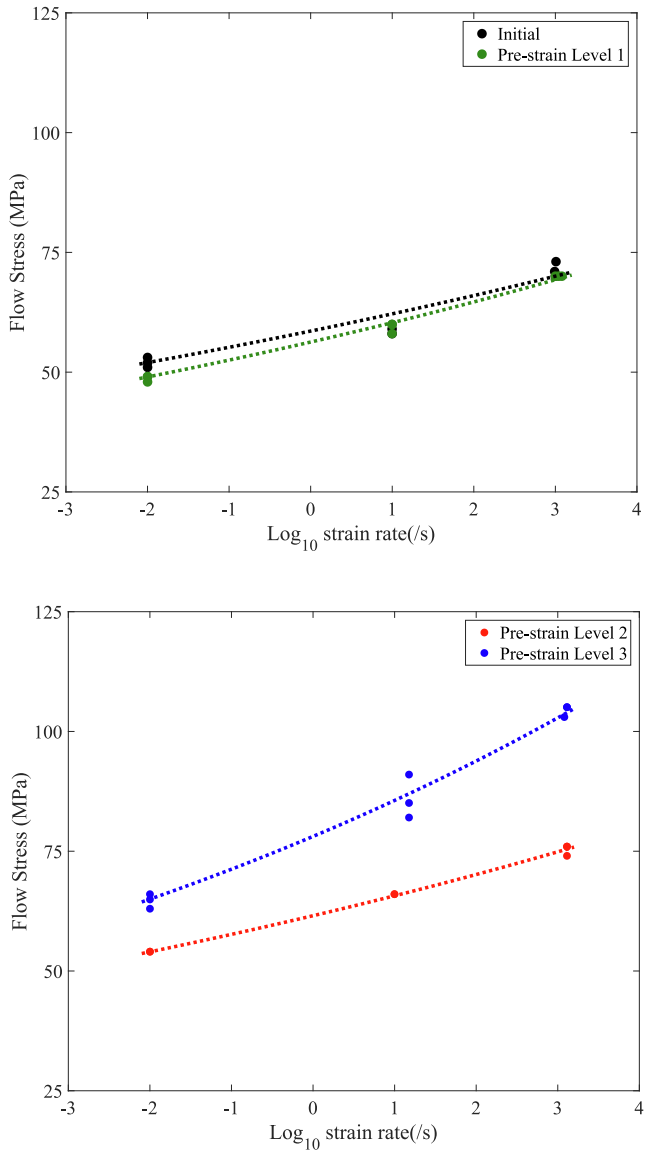

Fig. 13. Flow stress as a function of strain rate of (a-b) the initial ESF and the ESF with pre-strain level 1 (c-d) the ESF with pre-strain level 2 and level 3. The points are the experimental data and the dashed lines are the model descriptions.

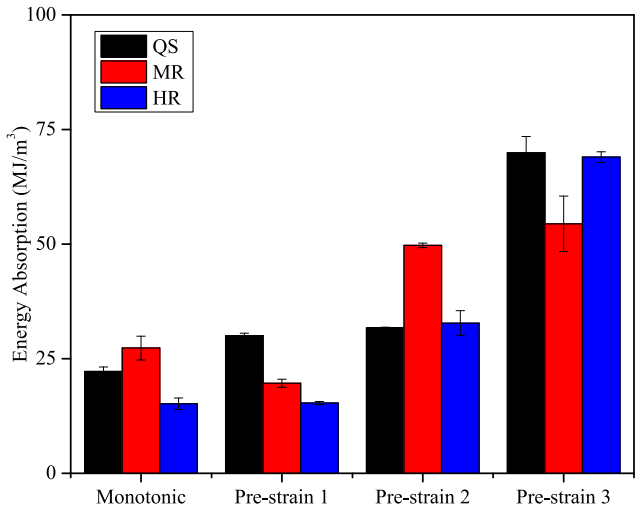

Fig. 14. Energy absorption vs strain rate of the initial ESF and the pre-strained ESF. The average values with the corresponding standard error are shown at quasi-static (QS), medium rate (MR) and high strain rate (HR).

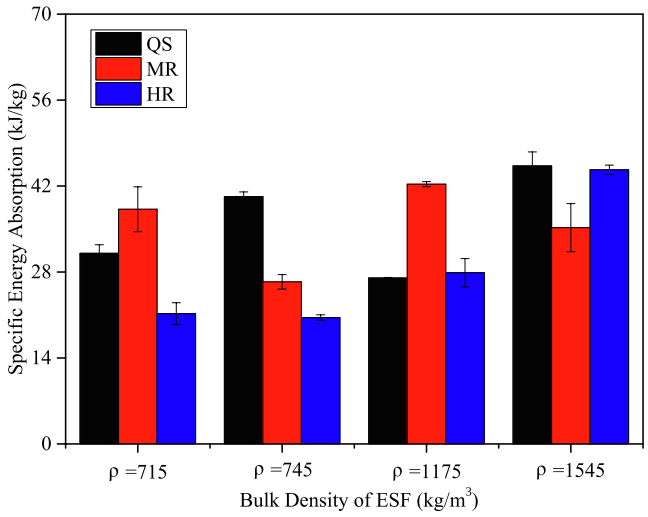

Fig. 15. Specific energy absorption vs strain rate of the ESF with different densities. The average values with the corresponding standard error are shown at quasi-static (QS), medium rate (MR) and high strain rate (HR).

of pre-strain. Likewise, the constitutive relationships of the pre-strained ESF are characterized from quasi-static to high strain rates.

A confinement technique is adopted to produce the pre-strained ESF (Fig. 1). A similar method was used by Kully [38], Liu and Subhash [37] for the study of the energy absorption of the pre-strained foam with confinement. Although the pre-strained foam of Liu and Subhash [37] was pushed out of the confinement tube for visual observation, the microstructure and mechanical properties of this pre-strained foam were not characterized further. The present paper studies the microstructure of the pre-strained ESF (Fig. 3 and Fig. 4). The microballons and the matrix are compacted, which results in a higher bulk foam density. Note that all the selected pre-strain levels provide the plastic deformation of ESF, which lead to failure of some microballons and their densification. In the initial stages, the space created by the fracture of microballons may be sufficient to accommodate compressive material and there may not be significant internal stresses generated because of the confinement. With the embeded colloapsed microballsons and the potentially absent internal stress, the ESF is subsequently subjected to the compressive loading from quasi-static to high strain rates.

The constant strain rate loading is an important technique to measure the mechanical properties of materials. The strain rate affects the deformation and failure of composite materials [65–68]. Based on the SHPB system, a pulse shaping technique, intensively used by Chen and Song [69], was adopted to achieve the compressive loading at constant strain rates of about 1000 /s. Likewise, the deformation of the ESF was monitored by using the high-speed photograph technique. The ESF specimens were slightly lubricated by grease, in order to reduce the friction between the interface of the specimen and the bars, a subject studied by Siviour and Walley [70]. These efforts enable accurate measurements of the stress–strain relationship of the initial and pre-strained ESF at high strain rates.

The slope of the initial part of the stress–strain curves of the ESF is influenced by the pre-strain (Fig. 9). This is similar to the observation of Kim et al. [36,71]. This initial part of ESF is governed by the volume fraction of the microballon, according to the recent studies of Carolan et al. [21], Huang and Li [72,73] The collapsed microballons in the pre-strained ESF affect the slope of the initial part in the stress–strain curve. Although the pre-strained foam was suggested as a fresh foam with a

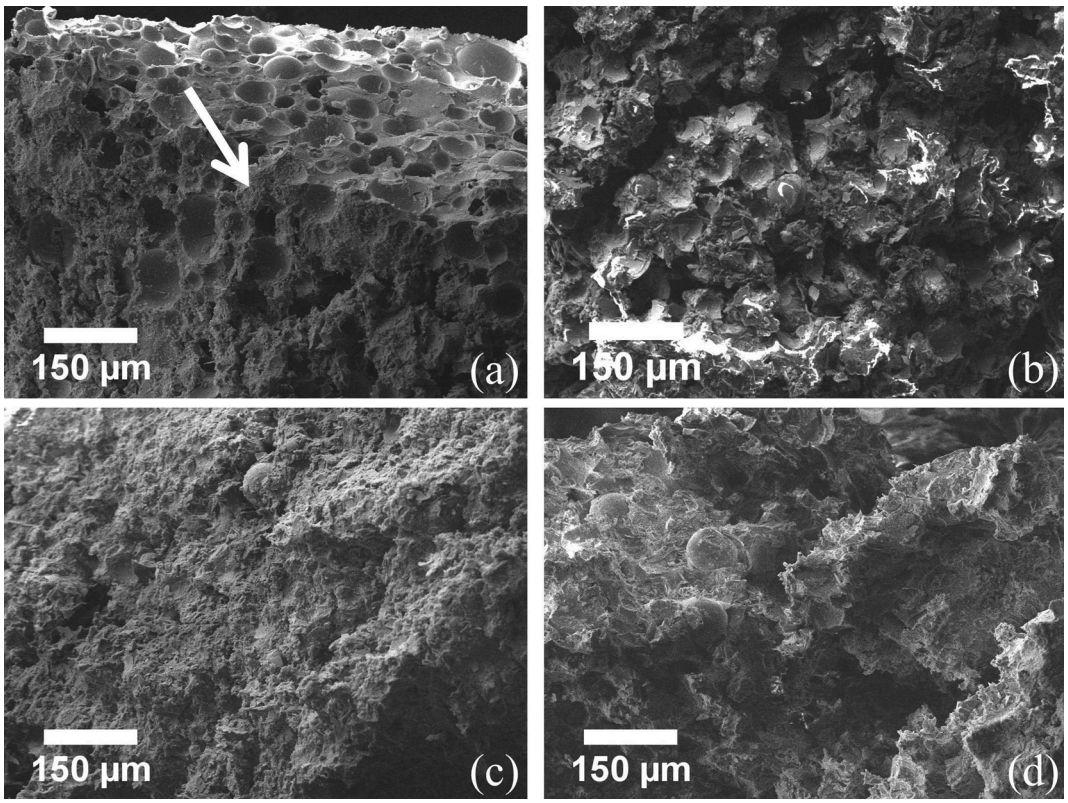

Fig. 16. Fracture morphology of the dynamically failed ESF (a) initial ESF (b) ESF with pre-strain level 1 (c) ESF with pre-strain level 2 (d) ESF with pre-strain level 3.

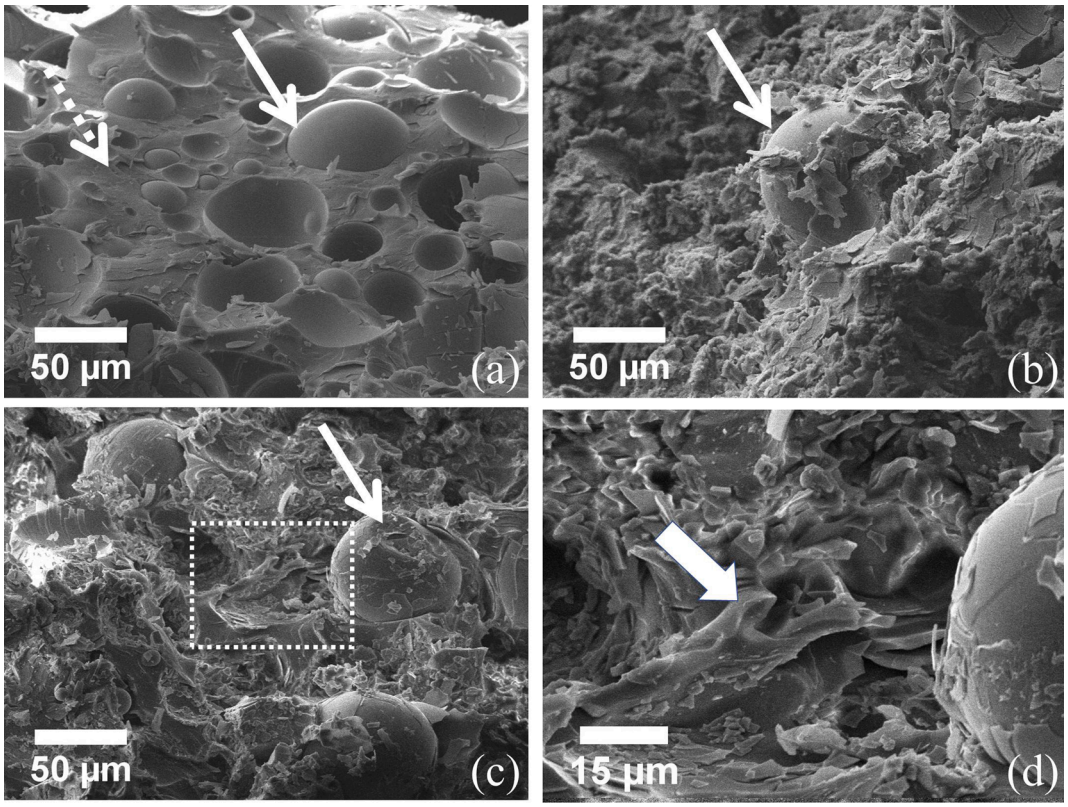

Fig. 17. Fracture morphology at a higher level of magnification (a) initial ESF (b) ESF with pre-strain level 2. The microballon is arrowed. (c) ESF with pre-strain level 3. The microballon is arrowed. (d) Magnified dashed rectangle area in (c).

higher bulk density [37], the present work clearly shows that, the pre-strained foam is actually not equivalent to a fresh foam, due to the damaged microballons and the change of the initial part of the stress–-strain curve. In addition, the pre-strained ESF is more deformable, instead of the early strain localization of the initial ESF.

The dynamic deformation processes of the initial and pre-strained ESF are monitored by using the high speed DIC technique. A homogeneous deformation can be seen in the dynamically deforming initial ESF and pre-strained ESF. This macro observation confirms no micro cracks in the matrix of the pre-strained ESF (Fig. 3 and Fig. 4). The initial foam presents an elastic-brittle behaviour with a rapid drop, due to the early onset of crushing of the microballons [26,74]. In contrast, the pre-strained ESF can undergo larger strain deformation with a slight barreling, until the occurrence of intensive strain localization. For the initial ESF, the intact microballons are the constituents which bear most of the compressive loading [72,73]. In the pre-strained foam, however, the compacted microballons and matrix jointly play roles in carrying the applied loading. The macro responses of the pre-strained ESF show improved deformability and high energy absorption (Figs. 14-15). This is very different from the gradually deteriorated properties (such as the energy absorption) of the polyisocyanurate foam with pre-strain [36,71], which could be related to the type of matrix material [75,76].

As can be seen from the microstructural characterizations of the dynamically failed ESF in Fig. 16a, more microballons exist in the failed ESF without pre-strain. This is different from those in the pre-strained ESF with evenly distributed debris in Fig. 16(b-d). The existence of more microballons would cause an earlier brittle failure of the bulk material. The compacted microstructure in the pre-strained ESF prevents the crushing of the remaining microballons and suppresses the brittle failure. This can be observed in the fracture morphology of the pre-strained ESF in Fig. 17c. The remaining microballons are surrounded by the flow like matrix. The flow like characteristic indicates an intensive plastic deformation feature of the matrix, a point highlighted in the works of Rittel [33], Gupta et al. [35] and Orbulov et al. [77]. At high strain rates under adiabatic condition, the deforming polymeric matrix is associated with thermomechanical coupling, a subject studied by Trojanowski et al. [78], Rittel [79], Li and Lambros [80]. The thermomechanical conversion from the mechanical work of deforming matrix contributes to the energy absorption and the structural integrity of the pre-strain foam. This microstructural observation agrees with the macro response of the pre-strained ESF.

By considering the embedded collapsed microballons, this study provides additional information on the variation of fracture strength and the density issue of syntactic foam, as can be seen in the recent works of Carolan et al. [21] and Irven et al. [53]. From a practical point of view, the evaluation of the crushability of the pre-strained foam would be considered as a means to study the behaviour of the foam under large deformation. In addition, the syntactic foam with embedded collapsed microballons doesn't show significantly weak properties in terms of deformability and energy absorption capacity. However, the syntactic foam with collapsed microballons might affect the stiffness of the structural component. This issue is suggested to be addressed carefully. The study would provide insight into impact resistant structures for the engineering community.

5. Conclusion

This paper systematically compares the strain rate dependent constitutive responses and dynamic failure mechanism of the ESF without and with pre-strain. The main outcomes are as follows:

- Different types of pre-strained ESF are produced. The SEM and micro CT-scan characterizations show that the pre-strain loading results in the collapsed microballons without micro cracks in the matrix of the ESF.
- The stress–strain relationships of the pre-strained ESF show more significant strain rate dependence than that of the initial ESF.
- The initial ESF presents dynamic brittle behaviour due to the collapse of large microballons. The ESF with compacted microballons presents deformation capability instead of brittleness.
- At high strain rates, the pre-strained ESF deforms uniformly before the shear localization, regardless of the existence of the collapsed microballons.
- The microstructure shows partially deformed and localized regions in the dynamically failed ESF without pre-strain. However, the microstructure presents evenly crushed microballons surrounded by the matrix with flow like behaviour in the dynamically failed ESF with pre-strain.
- The thermomechanical conversion from the severely deformed matrix would play a role in the structural integrity and the energy absorption of the foam with pre-strain. This corresponds to the improved energy absorption capacity of the pre-strained ESF.
- The present work provides a better understanding of the final crushability of ESF for practical engineering applications, with the consideration of the embedded collapsed microballons through the carefully designed pre-loading.

CRediT authorship contribution statement

Longhui Zhang: Conceptualization, Methodology, Investigation, Visualization, Writing – original draft, Writing – review & editing. **David Townsend:** Resources, Writing - review & editing.

Declaration of Competing Interest

The authors declare that they have no known competing financial interests or personal relationships that could have appeared to influence the work reported in this paper.

Data availability

Data will be made available on request.

Acknowledgements

The authors acknowledge the continuing support from Rolls-Royce plc through the University Technology Centre. The assistance from Mr. S. Carter is appreciated. Dear Prof. N. Petrinic is acknowledged for the hunting equipment to smash the foam.

References

[1] Shutov FA. Syntactic polymer foams. Chromatography/foams/copolymers: Springer; 1986. p. 63-123.
[2] Gibson LJ. Cellular solids. MRS Bull 2003;28(4):270–4.
[3] Gibson LJ, Ashby MF. Cellular Solids: Structure and Properties. 2 ed. Cambridge: Cambridge University Press; 1997.
[4] Zhang X, Bai C, Qiao Y, Wang X, Jia D, Li H, et al. Porous geopolymer composites: A review. Compos A Appl Sci Manuf 2021;150:106629.
[5] Kumar SA, Ahmed KS. Compression behavior and energy absorption capacity of stiffened syntactic foam core sandwich composites. J Reinf Plast Compos 2013;32(18):1370–9.
[6] Kishore GN, Sankaran S. On the characterisation of syntactic foam core sandwich composites for compressive properties. J Reinf Plast Compos 1999;18(14):1347–57.
[7] Kelly M, Arora H, Dear JP. The comparison of various foam polymer types in composite sandwich panels subjected to full scale air blast loading. Procedia Eng 2014;88:48–53.
[8] Arora H, Hooper PA, Dear JP. Dynamic response of full-scale sandwich composite structures subject to air-blast loading. Compos A Appl Sci Manuf 2011;42(11):1651–62.
[9] Ashby MF, Medalist RM. The mechanical properties of cellular solids. Metall Trans A 1983;14(9):1755–69.
[10] Bunn P, Mottram J. Manufacture and compression properties of syntactic foams. Composites 1993;24(7):565–71.

[11] Gupta N, Woldesenbet E. Characterization of Flexural Properties of Syntactic Foam Core Sandwich Composites and Effect of Density Variation. J Compos Mater 2005; 39(24):2197–212.
[12] Gupta N, Woldesenbet E. Compressive fracture features of syntactic foams-microscopic examination. J Mater Sci 2002;37(15):3199–209.
[13] Gupta N, Pinisetty D, Shunmugasamy VC. Reinforced polymer matrix syntactic foams: effect of nano and micro-scale reinforcement: Springer Science & Business Media; 2013.
[14] Kim HS, Plubrai P. Manufacturing and failure mechanisms of syntactic foam under compression. Compos A Appl Sci Manuf 2004;35(9):1009–15.
[15] Wouterson EM, Boey FY, Hu X, Wong S-C. Specific properties and fracture toughness of syntactic foam: Effect of foam microstructures. Compos Sci Technol 2005;65(11–12):1840–50.
[16] Gupta N, Ricci W. Comparison of compressive properties of layered syntactic foams having gradient in microballoon volume fraction and wall thickness. Mater Sci Eng A 2006;427(1–2):331–42.
[17] Gupta N, Woldesenbet E. Microballoon wall thickness effects on properties of syntactic foams. J Cell Plast 2004;40(6):461–80.
[18] Doddamani M. Effect of surface treatment on quasi-static compression and dynamic mechanical analysis of syntactic foams. Compos B Eng 2019;165:365–78.
[19] Jayavardhan ML, Doddamani M. Quasi-static compressive response of compression molded glass microballoon/HDPE syntactic foam. Compos B Eng 2018;149: 165–77.
[20] Bharath Kumar B, Doddamani M, Zeltmann SE, Gupta N, Gurupadu S, Sailaja R. Effect of particle surface treatment and blending method on flexural properties of injection-molded cenosphere/HDPE syntactic foams. J Mater Sci 2016;51(8): 3793–805.
[21] Carolan D, Mayall A, Dear JP, Fergusson AD. Micromechanical modelling of syntactic foam. Compos B Eng 2020;183:107701.
[22] Hornig A, Böhm H, Modler N, Gude M. Novel Design Methods for Composite Structures under High-Strain-Rate Loading Conditions. J Fail Anal Prev 2019;19 (1):144–6.
[23] Ahmadi E, Atrian A, Fesharaki JJ, Montazerolghaem H, Saberi S. Experimental and numerical assessment of high-velocity impact behavior of syntactic foam core sandwich structures. Eur J Mech A Solids 2021;90:104355.
[24] Pickett AK, Pyttel T, Payen F, Lauro F, Petrinic N, Werner H, et al. Failure prediction for advanced crashworthiness of transportation vehicles. Int J Impact Eng 2004;30(7):853–72.
[25] Mouritz AP. Advances in understanding the response of fibre-based polymer composites to shock waves and explosive blasts. Compos A Appl Sci Manuf 2019; 125:105502.
[26] Li P, Petrinic N, Siviour CR, Froud R, Reed JM. Strain rate dependent compressive properties of glass microballoon epoxy syntactic foams. Mater Sci Eng A 2009;515 (1):19–25.
[27] Hopkinson B. A method of measuring the pressure produced in the detonation of high explosives or by the impact of bullets. Proc Royal Soc London Series A 1914; 89(612):411–3.
[28] Kolsky H. An investigation of the mechanical properties of materials at very high rates of loading. Proceedings of the physical society Section B. 1949;62(11):676.
[29] Quinn RM, Zhang LH, Cox MJ, Townsend D, Cartwright T, Aldrich-Smith G, et al. Development and Validation of a Hopkinson Bar for Hazardous Materials. Exp Mech 2020.
[30] He R, Gao Y, Cheng L, Cui H, Li Y. Fracture toughness for longitudinal compression failure of laminated composites at high loading rate. Compos A Appl Sci Manuf 2022;156:106834.
[31] Song B, Chen W, Yanagita T, Frew DJ. Confinement effects on the dynamic compressive properties of an epoxy syntactic foam. Compos Struct 2005;67(3): 279–87.
[32] Gupta N, Shunmugasamy VC. High strain rate compressive response of syntactic foams: Trends in mechanical properties and failure mechanisms. Mater Sci Eng A 2011;528(25):7596–605.
[33] Rittel D. Adiabatic shear failure of a syntactic polymeric foam. Mater Lett 2005;59 (14–15):1845–8.
[34] Anirudh S, Jayalakshmi CG, Anand A, Kandasubramanian B, Ismail SO. Epoxy/hollow glass microsphere syntactic foams for structural and functional application-A review. Eur Polym J 2022;171:111163.
[35] Gupta N, Luong DD, Rohatgi PK. A method for intermediate strain rate compression testing and study of compressive failure mechanism of Mg-Al-Zn alloy. J Appl Phys 2011;109(10):103512.
[36] Kim S-K, Kim J-H, Lee J-H, Park S-B, Lee J-M. Comparative study on mechanical behavior after deformation recovery of polymeric foam for ships and offshore structures. J Soc Naval Architects of Korea 2016;53(3):195–200.
[37] Liu Q, Subhash G, Gao X-L. A parametric study on crushability of open-cell structural polymeric foams. J Porous Mater 2005;12(3):233–48.
[38] Kully RM. Dynamic constitutive equation for a syntactic foam under multi-axial stress state. North Carolina Agricultural and Technical State University; 2014.
[39] Walker JD. From columbia to discovery: Understanding the impact threat to the space shuttle. Int J Impact Eng 2009;36(2):303–17.
[40] Walker J, Chocron S, Gray W. Computational and analytical modeling of foam, ice and ablator materials impacting space shuttle thermal tiles. 47th AIAA/ASME/ASCE/AHS/ASC Structures, Structural Dynamics, and Materials Conference 14th AIAA/ASME/AHS Adaptive Structures Conference 7th2006. p. 1779.
[41] Sutliff DL, Jones MG. Low-speed fan noise attenuation from a foam-metal liner. J Aircr 2009;46(4):1381–94.
[42] Sutliff DL, Jones MG, Hartley TC. High-speed turbofan noise reduction using foam-metal liner over-the-rotor. J Aircr 2013;50(5):1491–503.
[43] Horton B, Bayandor J. Numerical investigation of fan-blade out using meso-scale composite modeling. 30th Congress of the International Council of the Aeronautical Sciences, ICAS2016. p. 1-8.
[44] Rolls-Royce plc. The jet engine: John Wiley & Sons; 2015.
[45] Society IDIC. A good practices guide for digital image correlation. iDICs: International Digital Image Correlation society; 2018.
[46] Chen J, Guo B, Liu H, Liu H, Chen P. Dynamic Brazilian test of brittle materials using the split Hopkinson pressure bar and digital image correlation. Strain 2014; 50(6):563–70.
[47] Wang L, Foote KG, Theobald PD, Robinson SP. Material properties of three syntactic foams. OCEANS 2017-Aberdeen: IEEE; 2017. p. 1-6.
[48] Flores-Johnson E, Li Q. Indentation into polymeric foams. Int J Solids Struct 2010; 47(16):1987–95.
[49] Li P, Wang Z, Petrinic N, Siviour C. Deformation behaviour of stainless steel microlattice structures by selective laser melting. Mater Sci Eng A 2014;614: 116–21.
[50] Prabhakar P, Feng H, Subramaniyan SP, Doddamani M. Densification mechanics of polymeric syntactic foams. Compos B Eng 2022;232:109597.
[51] Gupta N, Zeltmann SE, Luong DD, Doddamani M. Testing of Foams. In: Schmauder S, Chen C-S, Chawla KK, Chawla N, Chen W, Kagawa Y, editors. Handbook of Mechanics of Materials. Singapore: Springer Singapore; 2019. p. 2083-122.
[52] Woldesenbet E, Gupta N, Jadhav A. Effects of density and strain rate on properties of syntactic foams. J Mater Sci 2005;40(15):4009–17.
[53] Irven G, Carolan D, Fergusson A, Dear JP. Fracture performance of epoxy foam: Low density to bulk polymer. Polymer 2022;261:125420.
[54] Joffre T, Miettinen A, Berthold F, Gamstedt EK. X-ray micro-computed tomography investigation of fibre length degradation during the processing steps of short-fibre composites. Compos Sci Technol 2014;105:127–33.
[55] Huang R, Li P, Wang Z, Liu T. X-Ray Microtomographic Characterization and Quantification of the Strain Rate Dependent Failure Mechanism in Cenosphere Epoxy Syntactic Foams. Adv Eng Mater 2016;18(9):1550–5.
[56] Gerlach R, Kettenbeil C, Petrinic N. A new split Hopkinson tensile bar design. Int J Impact Eng 2012;50:63–7.
[57] Zhang L. Thermo-mechanical characterization and dynamic failure of a CoCrFeNi high-entropy alloy. Mater Sci Eng A 2022;844:143166.
[58] Zhang L. Influence of shear stress state on dynamic fracture of a glass ceramic Macor. Ceram Int 2022;48(17):24582–91.
[59] Quino G, Tagarielli VL, Petrinic N. Effects of water absorption on the mechanical properties of GFRPs. Compos Sci Technol 2020;199:108316.
[60] Pan B, Asundi A, Xie H, Gao J. Digital image correlation using iterative least squares and pointwise least squares for displacement field and strain field measurements. Opt Lasers Eng 2009;47(7–8):865–74.
[61] GmbH L. Product-Manual for DaVis 8.3: Imaging Tools. LaVision GmbH Gottingen; 2015.
[62] Gupta N, Woldesenbet E, Sankaran S. Studies on compressive failure features in syntactic foam material. J Mater Sci 2001;36(18):4485–91.
[63] Song B, Chen W, Frew DJ. Dynamic Compressive Response and Failure Behavior of an Epoxy Syntactic Foam. J Compos Mater 2004;38(11):915–36.
[64] Sanborn B, Song B, Smith S. Pre-strain effect on frequency-based impact energy dissipation through a silicone foam pad for shock mitigation. Journal of Dynamic Behavior of Materials 2016;2(1):138–45.
[65] Schiffer A, Lee D, Kim E, Kim T-Y. Interaction of highly nonlinear solitary waves with rigid polyurethane foams. Int J Solids Struct 2018;152:39–50.
[66] Fenu L, Forni D, Cadoni E. Dynamic behaviour of cement mortars reinforced with glass and basalt fibres. Compos B Eng 2016;92:142–50.
[67] Hufenbach W, Langkamp A, Gude M, Ebert C, Hornig A, Nitschke S, et al. Characterisation of Strain rate Dependent Material Properties of Textile Reinforced Thermoplastics for Crash and Impact Analysis. Procedia Mater Sci 2013;2:204–11.
[68] Jia S, Wang F, Zhou J, Jiang Z, Xu B. Study on the mechanical performances of carbon fiber/epoxy composite material subjected to dynamical compression and high temperature loads. Compos Struct 2021;258:113421.
[69] Chen WW, Song B. Split Hopkinson (Kolsky) bar: design, testing and applications: Springer Science & Business Media; 2010.
[70] Siviour CR, Walley SM. Inertial and frictional effects in dynamic compression testing. The Kolsky-Hopkinson bar machine: Springer; 2018. p. 205-47.
[71] Kim S-K , Kim J-D , Lee D-H , Kim J-H , Lee J-M Characteristics of pre-strained polyisocyanurate foam: Deformation recovery and compressive mechanical behavior at cryogenic temperature . J. Cell. Plast 2022 ; 58 (2): 357 – 376.
[72] Huang R, Li P. Elastic behaviour and failure mechanism in epoxy syntactic foams: The effect of glass microballoon volume fractions. Compos B Eng 2015;78:401–8.
[73] Huang R, Li P, Liu T, Xu J. The 3D failure process in polymeric syntactic foams with different cenosphere volume fractions. J Appl Polym Sci 2019;136(19):47491.
[74] Subhash G, Liu Q, Gao X-L. Quasistatic and high strain rate uniaxial compressive response of polymeric structural foams. Int J Impact Eng 2006;32(7):1113–26.
[75] Li G, Jones N. Development of rubberized syntactic foam. Compos A Appl Sci Manuf 2007;38(6):1483–92.
[76] Van Belle B. Advances in high-temperature syntactic foam technology for offshore systems. Offshore Technology Conference: OnePetro 2002.
[77] Orbulov IN, Szlancsik A, Kemény A, Kincses D. Compressive mechanical properties of low-cost, aluminium matrix syntactic foams. Compos A Appl Sci Manuf 2020; 135:105923.

[78] Trojanowski A, Ruiz C, Harding J. Thermomechanical properties of polymers at high rates of strain. Le Journal de Physique IV. 1997;7(C3):C3-447-C3-52.
[79] Rittel D. On the conversion of plastic work to heat during high strain rate deformation of glassy polymers. Mech Mater 1999;31(2):131–9.
[80] Li Z, Lambros J. Dynamic thermomechanical behavior of fiber reinforced composites. Compos A Appl Sci Manuf 2000;31(6):537–47.